Partial dislocations at domain intersections in a tetragonal ferroelectric crystal

2004 J. Phys.: Condens. Matter 16 1455

(http://iopscience.iop.org/0953-8984/16/8/026)

INSTITUTE OF PHYSICS PUBLISHING JOURNAL OF PHYSICS: CONDENSED MATTER

J. Phys.: Condens. Matter **16** (2004) 1455–1466 PII: S0953-8984(04)72915-X

Partial dislocations at domain intersections in a tetragonal ferroelectric crystal

X Tan[1] **and J K Shang**[2]

[1] Department of Materials Science and Engineering, Iowa State University, Ames, IA 50011, USA
[2] Department of Materials Science and Engineering, University of Illinois at Urbana-Champaign, Urbana, IL 61801, USA

Received 2 December 2003
Published 13 February 2004
Online at stacks.iop.org/JPhysCM/16/1455 (DOI: 10.1088/0953-8984/16/8/026)

Abstract

Domain behaviour under electric cycling was examined by transmission electron microscopy in a ⟨001⟩-oriented $0.65Pb(Mg_{1/3}Nb_{2/3})O_3$–$0.35PbTiO_3$ ferroelectric crystal. Prior to electric cycling, the crystal contained two nonparallel sets of 90° domain walls along the two {110} planes. For the most part, the domain walls remained planar, dividing the crystal into highly regular domain strips. As two nonparallel domain walls approached each other, the domain width tapered down to avoid full contact. Upon repeated electric cycling, the domains were forced into full contact, resulting in direct intersections of 90° domain walls and charged wall segments along the domain intersection. At the domain intersection, partial dislocations were observed along with a stacking fault on a $\{\bar{1}01\}$ plane. These dislocations had a Burgers vector of $\frac{1}{2}[101]$ and were of predominantly screw type. It is suggested that the partial dislocations resulted from a shear displacement along [101] in the crystal as the domain switched its polarization to form the intersection.

1. Introduction

A ferroelectric domain represents a volume of a ferroelectric crystal in which uniform polarization, P, is found. The domain plays a central role in determining the ferroelectric properties of ferroelectric materials. Domains in ferroelectric crystals are formed to minimize the depolarization energy and elastic energy [1–3]. They are generally classified according to the configurations of the polarization vectors in the neighbouring domains [2]. In tetragonal crystals, the polarization vector is along one of their prototype cubic ⟨001⟩ directions, and the rotation of the polarization vector from one domain to the next can only be 90° or 180°. Therefore, 90° domains and 180° domains are found in tetragonal crystals. For rhombohedral crystals, the polarization vector is along ⟨111⟩, limiting the polarization configurations to 71°, 109°, and 180° domains.

Separating domains of different polarizations are domain walls or boundaries that are created when the domain wall energy W_w is balanced by the depolarization energy W_E, the dipolar energy W_{dip}, and the elastic energy W_x, as listed in equation (1) [1].

$$W_w = W_E + W_{dip} + W_x. \tag{1}$$

To minimize the dipolar energy, the polarization vectors are often arranged in the neighbouring domains so that div $P = 0$ at the wall. To maintain zero charge, domain walls are only permitted along certain sets of crystallographic planes. For the 90° domains in tetragonal crystals, domain walls are limited to {101} planes, with a head-to-tail arrangement of the dipoles at the wall. In rhombohedral crystals, the permissible crystallographic planes for the uncharged walls are {101} for 109° domains and {100} for 71° domains [4]. In both crystals, any plane parallel to the polarization vector is a permissible uncharged wall for 180° domains.

When a domain wall is tilted away from the permissible uncharged orientation, it will carry electric charges [5]. Indeed charged walls have been observed experimentally [5–7] and some of the common charged walls are depicted in figure 1. In figures 1(a) and (b), a charged 90° domain wall and a charged 180° wall are shown after these walls are rotated by a tilt angle θ away from the uncharged positions indicated by the dashed line. The charge density is $\sqrt{2}P \sin\theta$ for the 90° wall and $2P \sin\theta$ for the 180° wall, respectively. When a 90° domain wall tilts 90° away from the permissible uncharged position, the original head-to-tail arrangement of the polarization vectors will turn into a head-to-head arrangement and the wall attains the maximum charge density. In this case, the domain wall takes a saw-toothed morphology in order to restore the head-to-tail configuration [8], as depicted in figure 1(c). However, it is to be noted that the saw-toothed structure does not change the total electric charges, but dilutes the charge density by increasing the domain wall area.

Charged domain walls may also form when domain walls of different orientations intersect. Krishnan *et al* [5] recently analysed one such condition where two perpendicular sets of 90° domain strips meet. Figure 2 depicts the three possible intersection configurations of domains with in-plane polarization vectors. In figure 2(a), the impinging domain D_i and the approaching domain D_a come into full contact to form a 180° domain wall segment. This segment is tilted 45° away from its neutral position and thus charged with a density of $\sqrt{2}P$. The charge density along the intersection can be reduced if the approaching domain assumes a pointed tip as shown in figure 2(b) or eliminated if a step is added to the domain wall of the impinging domain as depicted in figure 2(c). However, the extra step in figure 2(c) introduces severe lattice distortion, resulting in high elastic energy at the intersection. With a smaller charge density and a lower elastic energy, the point contact configuration shown in figure 2(b) is therefore considered highly favourable in ferroelectric crystals for 90° domain intersections [5].

In this study, intersections of 90° domain walls produced by electric cycling were examined in a $0.65Pb(Mg_{1/3}Nb_{2/3})O_3$–$0.35PbTiO_3$ single crystal. With repeated electric cycling, segmental contact of 90° domains was found as two sets of domain strips were forced to intersect. At the intersection, the domain wall became deformed (bent) and partial dislocations were observed. Both the type and Burgers vector of the dislocations were determined. A possible mechanism for development of partial dislocations is suggested.

2. Experimental procedure

The ferroelectric system used in this study was a single crystal of $0.65Pb(Mg_{1/3}Nb_{2/3})O_3$–$0.35PbTiO_3$ (0.65PMN–0.35PT). The crystal was grown by a vertical Bridgman method in a sealed platinum crucible using (110) seeding. The crystal growth rate was 0.8 mm h^{-1} at a temperature gradient of 20 °C cm^{-1}. The as-grown crystal had a dark yellow green colour

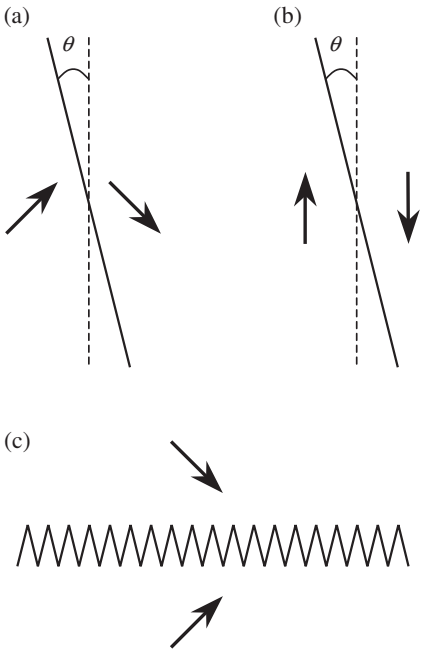

Figure 1. Charged domain walls in ferroelectric crystals with tetragonal structure: (a) a 90° domain wall; (b) a 180° domain wall; (c) a saw-toothed morphology taken by a 90° domain wall to resume the head-to-tail arrangement locally.

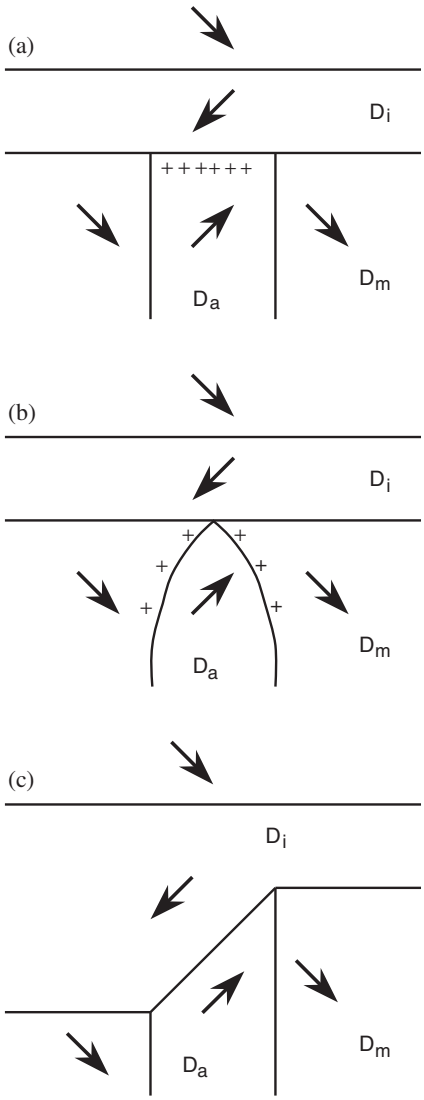

Figure 2. Intersections of 90° domains in ferroelectric crystals with tetragonal structure: (a) the approaching domain (D_a) is in full contact with the impinging domain (D_i); (b) D_a has a pointed tip; (c) a step is formed on the impinging-domain wall. D_m refers to the matrix domain.

and contained twins when examined under an optical microscope. X-ray diffraction analysis indicated that the crystal had a tetragonal structure.

Domain structures of the crystal were examined in a transmission electron microscope (TEM). TEM specimens of 3 mm diameter discs were ultrasonically cut from a {001} thin slice of the crystal, ground and polished to a thickness of $\sim$120 μm. The central areas of the discs were further thinned to about 15 μm by mechanical dimpling, then the specimens were annealed at 250 °C for 1 h to remove residual stresses. Two half-circle shaped Au films were evaporated on the flat surface of the dimpled sample with a gap of about 500 μm parallel to

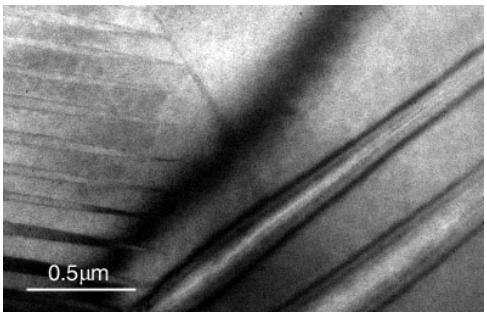

Figure 3. The initial domain configurations in a 0.65PMN–0.35PT single crystal prior to the application of electric fields. The *a*-domains and *c*-domains coexisted but stayed apart.

the ⟨100⟩ direction. Bipolar cyclic electric fields were applied to the electroded sample at an amplitude of ± 6.5 kV cm^{-1} for 5×10^6 cycles. The electrically cycled sample was then ion milled at 5 kV with 12° incidence angle until the occurrence of a central perforation. Domain and dislocation observations were carried out in a Phillips CM-12 TEM operated at 120 kV.

3. Results

3.1. Initial domain structure

Prior to electric cycling, the initial domain structure of the crystal consisted of alternating dark/bright strips aligned along {110} planes of the crystal. Convergent beam electron diffraction analysis indicated that these strips were 90° domains since the mirror planes in two neighbouring domains were perpendicular to each other. As shown in figure 3, one set of the domain strips tapered down to pointed tips when they approached another set of strips oriented along a different {110} plane. The pointed tip configuration has also been observed in other ferroelectric crystals [5, 7, 9] and is believed to be the energetically favourable configuration. Extensive examination of many TEM specimens from this crystal indicated that the crystal was dislocation-free in the as-grown state. Evidently, the creation of 90° domains was effective in relieving the internal strain developed during crystal growth.

To distinguish different sets of domains in thin foil tetragonal crystals, it is common to denote domains with in-plane polarization vectors as *a*-domains and those with out-of-plane polarization vectors as *c*-domains [7]. Figure 4 illustrates the possible combinations of 90° *a*–*c* domains with permissible uncharged walls. In this particular crystal orientation, an *a*-domain is surrounded by either an *a*-domain matrix or a *c*-domain matrix, but a *c*-domain can only be housed in an *a*-domain matrix. The domain wall between the two orthogonal *a*-domains in figure 4(a) is parallel to a $\{\bar{1}10\}$ plane (all the plane and direction indices are based on the parent cubic structure), whereas the wall between the *a*- and *c*-domains in figures 4(b) and (c) has indices of $\{\bar{1}01\}$. All the illustrations in figures 1 and 2 are based on *a*-domains for the sake of simplicity, but should apply equally to *c*-domains.

In a TEM, the *a*/*a*-domain wall creates the contrast of a thin line but the inclined *a*/*c* domain wall produces fringes in the image contrast. According to the notation in figure 4, the domains in figure 3 belong to three different sets. The set of the domains with pointed tips in figure 3 are *a*-domains. They are separated by another set of *a*-domains which is referred to as the matrix domain. The third set share inclined domain walls with the matrix domains and therefore are *c*-domains. The entire domain structure may be taken as a mixture

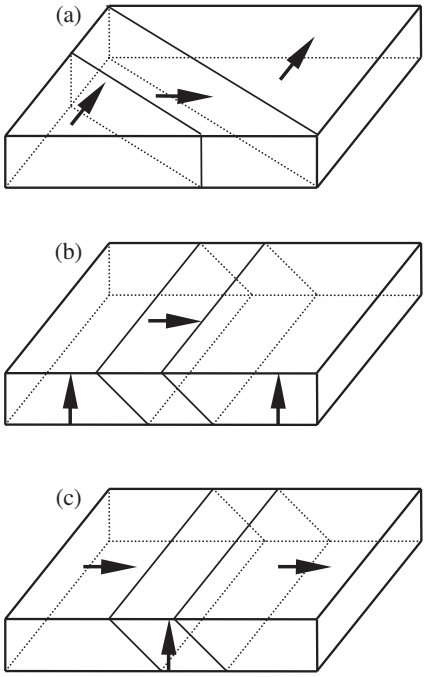

Figure 4. Schematic diagrams for *a*- and *c*-domains in an {001} thin foil of tetragonal crystals. (a) An *a*-domain in an *a*-domain matrix; (b) an *a*-domain in a *c*-domain matrix; (c) a *c*-domain in an *a*-domain matrix.

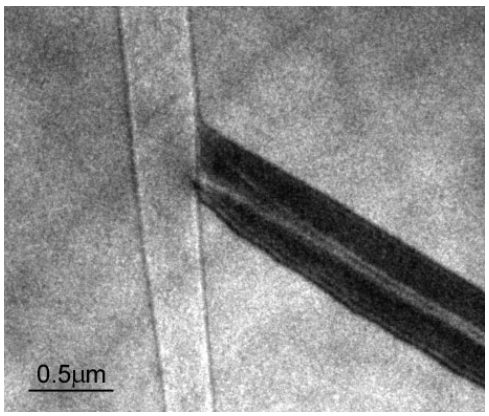

Figure 5. The domain morphology of an electrically cycled crystal. The *a*-domain was forced to grow and was impinged by the retracting *c*-domain. The electron beam direction is close to [001].

of *a*-domains and *c*-domains inserted in a matrix of *a*-domains. Although *a*-domains and *c*-domains coexisted, they tended to stay away and occupy separate volumes in the crystal.

3.2. Domain intersections

Upon the application of an electric field above the coercive field along an in-plane ⟨010⟩ direction, *a*-domains grew and *c*-domains diminished. The associated domain wall movement

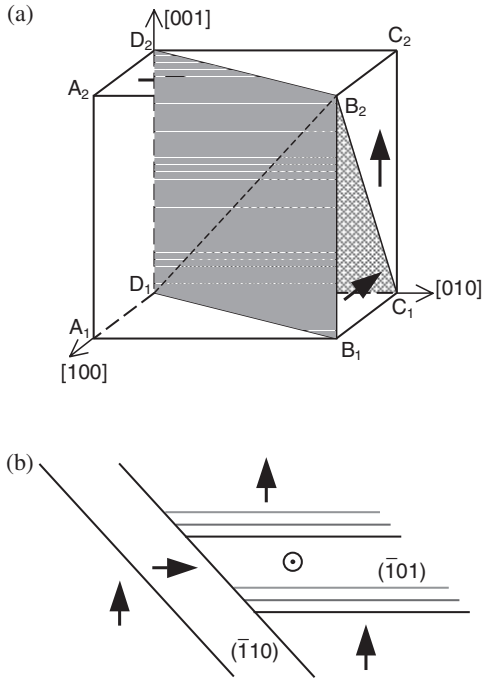

Figure 6. The intersection of an *a*-domain and a *c*-domain. (a) Three-dimensional illustration of the intersection; (b) the projected view of the intersection shown in (a).

Table 1. Possible combinations of an *a*-domain intersecting with a *c*-domain in the *a*-domain matrix.

a/*a* domain wall	$(\bar{1}10)$	$(\bar{1}10)$	$(\bar{1}10)$	$(\bar{1}10)$	(110)	(110)	(110)	(110)
a/*c* domain wall	(011)	$(0\bar{1}1)$	$(\bar{1}01)$	(101)	(011)	$(0\bar{1}1)$	$(\bar{1}01)$	(101)

resulted in impingement of the *a*- and *c*-domains, as shown in figure 5. Unlike the point contact seen previously, the contact between the two domains was extended to the entire width of the *c*-domain. Very close to the intersection, the wall of the *c*-domain was deformed to bend outward on the far side, as opposed to an inward curvature typical of a tapered domain tip. The impinging *a*-domain appeared relatively undisturbed. When straight lines were drawn along the central plane of the two domains, the angle between the two central lines was roughly 55°.

Based on the crystallographic orientations of the polarization vector and domain wall in tetragonal ferroelectric crystals, it is determined that the domain intersection in figure 5 may be related to any of the eight possible combinations of *a*- and *c*-domains with the domain walls along those {110} planes listed in table 1. To analyse the crystallography of the intersection, Figure 6 presents a schematic representation of the planes and directions involved with one set of those combinations. In figure 6(a), the prism $A_1B_1D_1$–$A_2B_2D_2$ is the *a*-domain with polarization vector along [010] direction, the tetrahedron B_2–$B_1C_1D_1$ is the matrix *a*-domain with polarization vector along $[\bar{1}00]$ direction, and the pyramid B_2–$D_1C_1C_2D_2$ is the *c*-domain with polarization vector along [001] direction. The domain walls $D_1B_1B_2$ and $D_1C_1B_2$ separate the *a*- and *c*-domains from the matrix domain. Both remain uncharged before and after the intersection. The intersecting plane $D_1B_2D_2$ between the *a*-domain and the *c*-domain is also a 90° domain wall; however, it carries electric charges because it is tilted away from its neutral

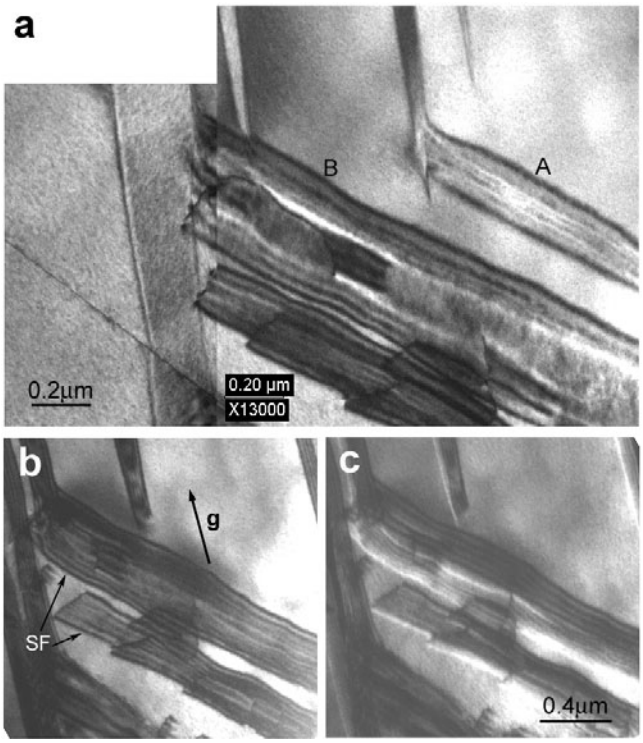

Figure 7. Partial dislocations and stacking faults in the electrically cycled specimen. (a) Domains 'A' and 'B' are *c*-domains with domain walls on the $(\bar{1}01)$ plane. Stacking faults were extended on the same set of $(\bar{1}01)$ planes. $\mathbf{B} \parallel [00\bar{1}]$. (b) Bright field image, $\mathbf{g} = \bar{1}10$, $\mathbf{B} \parallel [22\bar{3}]$. (c) Dark field image.

position. When viewed along the $[00\bar{1}]$ direction, the projected image of the intersection in figure 6(a) is as shown in figure 6(b).

If the crystal were cubic, the TEM image of the domain intersection in figure 5 should match the domain configuration in figure 6(b). Under this assumption, the angle between the walls of two intersecting domains should be 60° for all eight possible combinations in table 1. On the $[00\bar{1}]$ projection, the intersection angle should be 45° in figure 6(b). The deviation of the intersection angle in the TEM image of figure 5 from 45° suggests that the lattice near the intersection had been distorted as the tetragonal ferroelectric domains were forced to intersect. Based on the difference in the intersection angle between the TEM image and figure 6(b), the distortion strain was estimated to be more than a few per cent.

3.3. Partial dislocations

One way to relieve the intense lattice distortion at the domain intersection is to induce fracture of the crystal. This has indeed been observed but will be treated separately [10]. Another way for the strain relief is through dislocations. Dislocations formed at the domain intersection in the electrically cycled crystal are shown in figure 7. In figure 7(a), *a*-domains are running up and down in the micrograph, while the two *c*-domains (labelled 'A' and 'B') extend from the lower-right to the upper-left. The matrix is an *a*-domain. The partial dislocations apparently lay on the planes parallel to the inclined domain wall planes: $(\bar{1}01)$, according to the notation of figure 6.

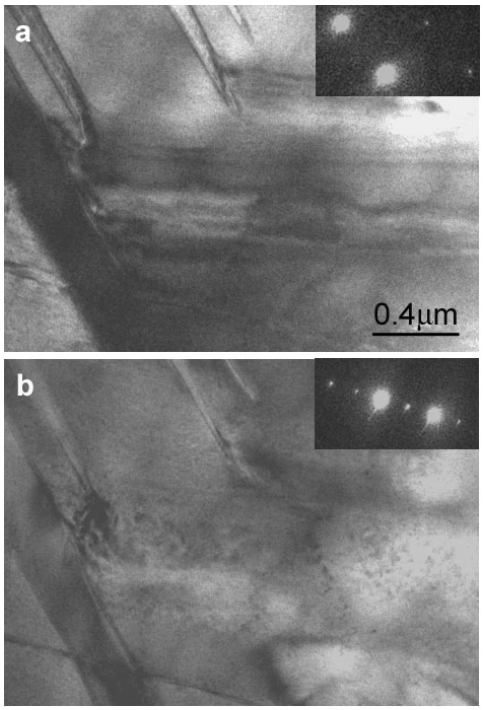

Figure 8. Partial dislocations contrast at two invisible conditions. (a) $\mathbf{g} = 1\bar{2}\bar{1}$, $\mathbf{B} \parallel [13\bar{5}]$; (b) $\mathbf{g} = 020$, $\mathbf{B} \parallel [00\bar{1}]$.

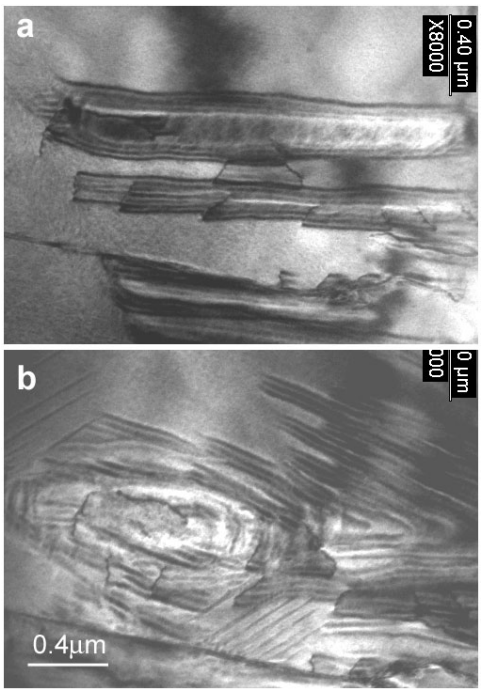

Figure 9. Electron beam radiation effects on partial dislocations. (a) Initial configurations; and (b) after 3 min radiation at beam current of 500 nA.

Table 2. Contrast of partial dislocations under various diffraction conditions.

020	$\bar{2}00$	$\bar{1}10$	$\bar{1}\bar{1}0$	$21\bar{1}$	$1\bar{2}\bar{1}$	$\bar{2}\bar{1}2$
Invisible	Visible	Visible	Visible	Visible	Invisible	Invisible

The same area was imaged under the two beam conditions with the diffraction vector $\mathbf{g} = \bar{1}10$, and the bright and dark field images are shown in figures 7(b) and (c). The fringes marked 'SF' represent stacking faults, which are always associated with partials dislocations. The presence of the domain B contrast in figures 7(b) and (c) and the absence of any contrast for domain A suggests that some partial dislocations and their associated stacking faults were collocated on the wall of domain B.

The Burgers vector of these partial dislocations was analysed by a series of diffraction contrast experiments. Although caution should be taken in using the $\mathbf{g} \cdot \mathbf{b} = 0$ invisibility criterion for Burgers vector determination in ferroelectric perovskites, practices of this criterion by the previous researchers demonstrated its applicability in ferroelectric crystals and obtained satisfactory results [11–14]. The same procedure was followed in this study and the results are listed in table 2. Figure 8 shows the dislocation contrast at invisible conditions. The Burgers vector for these partials was then assigned as $\frac{1}{2}[101]$, lying on the stacking fault plane $(\bar{1}01)$. Since the dislocation lines were close to their Burgers vector direction, these partial dislocations had a predominant screw character.

3.4. Dislocation mobility

The relative mobility of the partial dislocations in figure 7 was examined by radiating the dislocated area in the TEM specimen with a focused electron beam at different currents and for different times. The beam current was estimated from the automatic exposure time displayed on the microscope's control panel for emulsion films. After 15 min radiation at each beam current of 5, 17, and 30 nA, no visible change to the dislocation configuration and domain structure was observed. When the beam current was increased to about 500 nA, exposure of the area to the focused electron beam for about 3 min caused a drastic change of the domain structure, as shown in figure 9. As a result, a complex domain pattern emerged as the radiation heating raised the local temperature close to or above the Curie temperature (around 150 °C for this crystal) and mechanical stresses developed from non-uniform thermal strains in the heated area. However, despite the intense heating, the location and configuration of the partial dislocations remained unchanged when figure 9(a) was compared to figure 9(b), indicating that the partial dislocations were quite stable or locked in with the domain intersection. Such a stable dislocation structure is in sharp contrast to a previous study on $BaTiO_3$ crystals, where the dislocation configurations were found to be easily altered by electron beam radiation [15].

4. Discussion

The TEM observations of the electrically cycled PMN–PT crystal have shown that 90° domains can be forced to intersect with full contact of the two intersecting domains even though the contact results in a charged domain wall along the intersection. The formation of such a domain intersection requires polarization switching and induces severe lattice distortion [16]. The required polarization switching may be achieved by a shear displacement along $\langle 101 \rangle$, which may be accommodated by the development of extended dislocations with Burgers vector of $\frac{1}{2}\langle 101 \rangle$ type, as follows.

4.1. Polarization switching

Consider the formation of an intersection between a *c*-domain and an *a*-domain in the matrix of another *a*-domain, as shown in figure 6(b). Prior to intersection, these two domains were separated by the matrix *a*-domain. Under the influence of the applied electric field along an in-plane $\langle 010 \rangle$ direction, the *a*-domain expanded because of its favoured polarization direction while the *c*-domain contracted due to unfavoured direction. Assume the *a*-domain grew faster and the retraction of the *c*-domain lagged behind and an intersection resulted. This assumption is reasonable because the *a*-domain growth involved in-plane polarization rotation while the retraction of the *c*-domain proceeded via switching the out-of-plane polarization along [001] to the in-plane $[\bar{1}00]$ polarization.

The polarization switching may occur gradually by continuous rotation of the polarization vector. The lattice rotation would result in large lattice distortion, leading to domain fracture near the intersection [10]. Alternatively, domain switching may proceed through a shear displacement of the lattice as shown in figure 10, which depicts the atomic arrangements on plane $B_1C_1C_2B_2$ in the cubic construction of figure 6(a). To convert the *c*-domain into the matrix *a*-domain, the shear displacement is along B_2C_1 direction [101] on the *a*/*c* domain wall plane $(\bar{1}01)$.

Compared to the gradual lattice rotation, the shear displacement of the lattice would require a larger driving force. In cases of the domain intersection observed in figures 5 and 7, the severe lattice strain developed in the early advances of the *a*-domain toward the *c*-domain

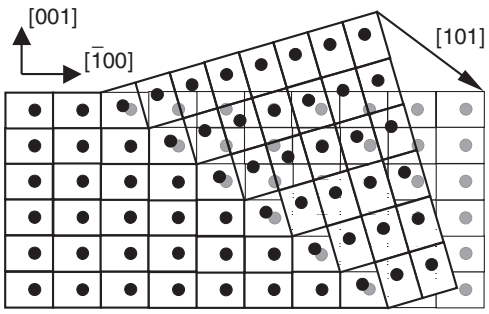

Figure 10. A schematic diagram of 90° domain switching to convert the *c*-domain to the matrix *a*-domain.

would provide additional driving force beside the applied field. Under repeated electric cycling, the lattice displacements along [101] during 90° domain switching may serve as precursors for the nucleation of $\frac{1}{2}$[101] partial dislocations. Moreover, the high compressive stress developed when the *c*-domain is compressed against the *a*-domain, as shown by the outward curvature of the domain wall on the far side of the *c*-domain in figure 5, would also favour a deformation-type mechanism rather than domain fracture.

4.2. Partial dislocations

Deformation of crystals with a perovskite structure by dislocation glide has been observed in $SrTiO_3$ [12, 13, 17–19], $BaTiO_3$ [11, 15, 20, 21], and $Pb(Zr, Ti)O_3$ [14, 16, 22]. In the cubic perovskite structure, the shortest Burgers vector of a perfect dislocation is ⟨100⟩, and ⟨101⟩ is the second shortest. Burgers vectors of ⟨101⟩, and ⟨100⟩ with slip planes of {100}, {101}, and {211} have been reported in ABO_3 perovskites [13, 14, 17, 21]. Among these, the {101} ⟨101⟩ system is probably the most often observed system. Crystallographic analysis shows that this system is the only one that would not bring cations close to each other during dislocation glide [21].

While dislocations with slip systems {101} ⟨101⟩ would produce the necessary shear displacement in figure 10, they are not as energetically favourable as, and tend to dissociate into, partial dislocations of Burgers vector $\frac{1}{2}$⟨101⟩ by the following reactions:

$$\langle 101\rangle \rightarrow \tfrac{1}{2}\langle 101\rangle + \tfrac{1}{2}\langle 101\rangle. \tag{2}$$

In fact, dissociation of a perfect ⟨101⟩ or ⟨001⟩ dislocation into two $\frac{1}{2}$⟨101⟩ partials has often been observed in perovskite crystals [11–14, 21]. Therefore, lattice distortion associated with the shear displacement required in figure 10 for domain switching may be effectively relieved by the formation of partial dislocations with Burgers vector $\frac{1}{2}$⟨101⟩ on the ($\bar{1}$01) plane.

Since the PMN–PT crystal contained mixed ions, rearrangement of anions and cations following a ($\bar{1}$01)–$\frac{1}{2}$[101] translational displacement is shown in figure 11. The dashed line in figure 11(a) indicates the ($\bar{1}$01) plane which includes the layers consisting entirely of O-only ⟨101⟩ rows. On these layers a *half* of the full lattice vector, $\frac{1}{2}$[101], denoted by the arrow along the dashed line, makes up an identical translation. This observation led to the suggestion that the half partials dissociated from a perfect [101] dislocation according to equation (2) might climb onto the nearest glide plane, denoted as L1 and L3 layers, on the other side of the O-only layer L2, to provide an easy slip mechanism in the perovskites [12]. In this way, the BO_6 octahedra are preserved and linked by common edges at the ($\bar{1}$01) fault plane. An 'out

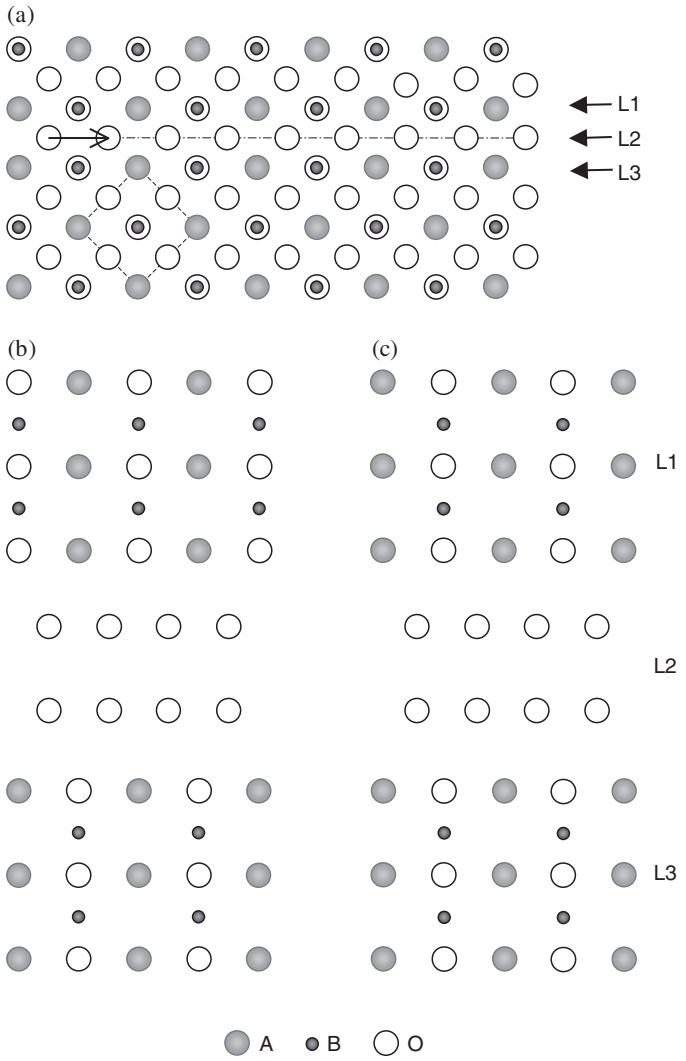

Figure 11. Schematic illustration of cations and anions packing sequence around the $(\bar{1}01)$–$\frac{1}{2}[101]$ partial dislocations in ABO_3 crystals. (a) Projections along $[0\bar{1}0]$ direction. (b) Ion arrangement on (101) plane component layers of L1, L2 and L3 in ideal crystal; and (c) the same layers after the occurrence of stacking fault.

of phase' arrangement in the cation sublattices is produced (compare figures 11(b) and (c)), and the fault may be regarded, therefore, as an antiphase boundary [14]. Such dissociation on anion-only layers in the perovskite structure accounted well for the observed stacking faults in our electrically cycled PMN–PT crystal.

5. Conclusions

A TEM study was carried out on an electrically cycled PMN–PT crystal. Electric cycling was found to induce intersections of 90° domain walls with different orientations. Along the intersection, full contact of the two domains was extended to the entire width of one domain.

The intersection produced charged domain walls, severe bending of the domain wall near the tip of the domain, and misorientation of the domain walls. In the vicinity of domain intersections, partial dislocations with Burgers vector $\frac{1}{2}[101]$ were observed lying on $(\bar{1}01)$ planes which coincided with the *a*/*c* domain walls. Crystallographic analysis indicated that partial dislocations could form as a mechanism to accommodate a shear displacement along [101] related to the switching of the *c*-domain to the matrix *a*-domain. It is shown that the stacking fault associated with the $(\bar{1}01)$–$\frac{1}{2}[101]$ partials produced an atomic arrangement that preserved the O-sublattice.

Acknowledgments

Support for this work was provided by the National Science Foundation under grant CMS-9872306. The TEM work was carried out in the Center for Microanalysis of Materials, University of Illinois, which is supported by the US Department of Energy under grant DEFG02-96-ER45439. One of the authors (XT) would also like to acknowledge the start-up support from Iowa State University.

References

[1] Lines M E and Glass A M 1977 *Principles and Applications of Ferroelectrics and Related Materials* (Oxford: Clarendon)
[2] Smolenskii G A 1984 *Ferroelectrics and Related Materials* (London: Gordon and Breach)
[3] Arlt G and Sasko P 1980 *J. Appl. Phys.* **51** 4956
[4] Ricote J, Whatmore R W and Barber D J 2000 *J. Phys.: Condens. Matter* **12** 323
[5] Krishnan A, Treacy M M J, Bisher M E, Chandra P and Littlewood P B 2000 *Fundamental Physics of Ferroelectrics 2000*; *AIP Conf. Proc.* **535** 191
[6] Lin P J and Bursill L A 1983 *Phil. Mag.* A **48** 251
[7] Hu Y H, Chan H M, Zhang X W and Harmer M P 1986 *J. Am. Ceram. Soc.* **69** 594
[8] Yakunin S I, Shakmanov V V, Spivak G V and Vasileva N V 1972 *Sov. Phys.—Solid State* **14** 373
[9] Suchicital C T A, Payne D A and de l'Eprevier A G 1986 *Int. Symp. Appl. Ferroeletrics* (Piscataway, NJ: IEEE) p 465
[10] Tan X, Shang J K and Han P 2004 at press
[11] Eibl O, Pongratz P, Skalicky P and Schmelz H 1988 *Phys. Status Solidi* a **108** 495
[12] Mao Z and Knowles K M 1996 *Phil. Mag.* A **73** 699
[13] Matsunaga T and Saka H 2000 *Phil. Mag. Lett.* **80** 597
[14] Prisedsky V V, Panko G F and Klimov V V 1985 *Ferroelectrics* **64** 257
[15] Bradt R C and Ansell G S 1967 *J. Appl. Phys.* **38** 5407
[16] Tsun Y F and Chou C C 1999 *Japan. J. Appl. Phys.* **38** 3585
[17] Brunner D, Taeri-Baghbadrani S, Sigle W and Ruhle M 2001 *J. Am. Ceram. Soc.* **84** 1161
[18] Gumbsch P, Taeri-Baghbadrani S, Brunner D, Sigle W and Ruhle M 2001 *Phys. Rev. Lett.* **87** 085505
[19] Chung S Y and Kang S J 2000 *J. Am. Ceram. Soc.* **83** 2828
[20] Dai Z R, Wang Z L, Duan X F and Zhang J 1996 *Appl. Phys. Lett.* **68** 3093
[21] Doukhan N and Doukhan J C 1986 *Phys. Chem. Minerals* **13** 403
[22] Esaklul K A, Gerberich W W and Koepke B G 1980 *J. Am. Ceram. Soc.* **63** 25